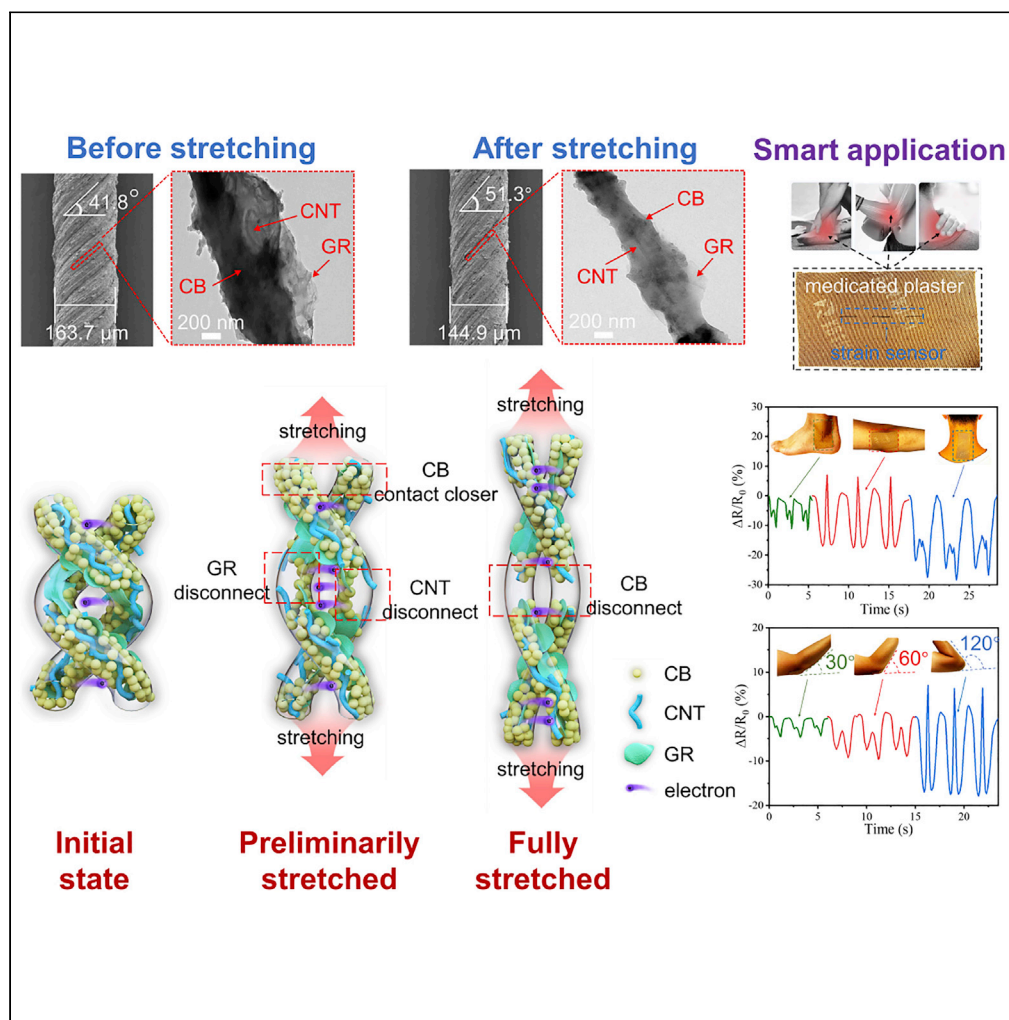**Article**

Sensing mechanism of a flexible strain sensor developed directly using electrospun composite nanofiber yarn with ternary carbon nanomaterials

Jian Tang, Yuting Wu, Shidong Ma, Tao Yan, Zhijuan Pan

yantao@suda.edu.cn (T.Y.)
zhjpan@suda.edu.cn (Z.P.)

Highlights

An anti-interference and washable strain-sensing composite nanofiber yarn

Synergy of carbon black particles, carbon nanotubes, and graphene flakes

Strain-sensing mechanism of ternary conductive networks are revealed

A smart medicated plaster can detect motions in the rehabilitation of joint pain

Article

Sensing mechanism of a flexible strain sensor developed directly using electrospun composite nanofiber yarn with ternary carbon nanomaterials

Jian Tang,[1] Yuting Wu,[1] Shidong Ma,[1] Tao Yan,[1,2,*] and Zhijuan Pan[1,2,3,*]

SUMMARY

Recently, various strain-sensing yarns have been developed without ideal stitchability. Herein, we used spherical carbon black particles (CBs), linear carbon nanotubes (CNTs), and lamellar graphene flakes (GRs) as conductive nanofillers to construct multi-element conductive networks inside a thermoplastic polyurethane (TPU) matrix. First, a highly stretchable and conductive multidimensional carbon-based nanomaterial/TPU composite nanofiber yarn was fabricated using electrospinning, which could be used as a flexible strain sensor without post-processing. Accordingly, the effects of nanomaterials' dimensionality and synergy on yarns' conductivity, mechanical properties, and strain sensing performances were explored. The yarn containing multiple networks formed by CB/CNT/GR ternary hybrid networks, CNT and GR auxiliary networks exhibited the best performances. Subsequently, the structural evolution of the ternary conductive network under stretching was revealed to further analyze the sensing mechanism. Finally, the yarn endowed a medicated plaster with an intelligent function to detect motions in the rehabilitation of joint pain by simple sewing.

INTRODUCTION

As indispensable elements of wearable electronic systems, flexible strain sensors have undergone significant development in recent years (Wu et al., 2021). Flexible strain sensors can convert various types of deformation into changes in electrical signals to detect the dynamic features of a physical state. According to the transition mechanism, they can be divided into resistance, capacitance, voltage, inductance, and magnetism types (Ma et al., 2022). Resistance-type sensors have significant advantages because of their simple preparation process, easy signal reception, and stable signal output (Liu et al., 2019a). They are usually fabricated by integrating conductive nanomaterials and flexible polymer matrices to form stretchable conductive networks (Liu et al., 2018a). Post-processing, like heat treatment and laser radiation, can enhance the conductivity of the network by reducing the contact resistance and increasing the number of contact points between the nanofillers in the polymer matrix (Ichkitidze et al., 2018, 2019).

The sensing mechanisms of resistance-type flexible strain sensors are that the number of electron transmission paths is changed at the macro-level because of the partial destruction and reconstruction of conductive networks under stretching (Kedambaimoole et al., 2020; Shi et al., 2020; Yan et al., 2019); The contact and tunneling resistance between the particles changed at the micro-level because of the displacement of the conductive nanomaterials (Wang et al., 2018; Yue et al., 2020; Zhao et al., 2019b).

The strain sensing range, sensitivity (defined as the gauge factor (GF), which is the ratio of the relative resistance change to the strain), as well as linearity, are the main performance indicators for flexible strain sensors (Zheng et al., 2020). The ideal electrical conductivity and mechanical properties are essential for a conductive nanomaterial/flexible matrix composite to be used as a sensing element. To obtain high-performance flexible strain sensors, researchers have mainly designed sensors based on two research directions: one is to design sensors with various kinds of geometric structures, such as one-dimensional (1D) fiber and yarn-like sensors, two-dimensional (2D) film and fabric-like sensors, and three-dimensional (3D) sponge, foam, and hydrogel-like sensors (Ma et al., 2022). These strain sensors have shown distinct performance characteristics and applications. Yarn-like strain sensors can be directly integrated into textiles through traditional textile technologies, which has aroused great interest in the field of smart clothing

[1]College of Textile and Clothing Engineering, Soochow University, Suzhou 215123, China

[2]National Engineering Laboratory for Modern Silk, Suzhou 215123, China

[3]Lead contact

*Correspondence: yantao@suda.edu.cn (T.Y.), zhjpan@suda.edu.cn (Z.P.)

https://doi.org/10.1016/j.isci. 2022.105162

(Wang et al., 2020). Compared with traditional yarns, nanofiber yarns have the advantages of large surface areas and high porosities, and they have been used in a wide range of surface-area-based applications, such as strain sensing (Yan et al., 2018).

The other direction is to use two or more conductive nanomaterials with different dimensions to design multi-element conductive networks. The synergistic effects between different conductive nanomaterials have been found to improve strain sensing performance. Zero-dimensional (0D) nanomaterials mainly contain carbon black particles (CBs) (Liu et al., 2018b) and metal nanoparticles (Qureshi et al., 2019). The 1D nanomaterials are principally carbon nanotubes (CNTs) (Ma et al., 2018), metal nanowires (Song et al., 2019), and carbon nanofibers (Lee et al., 2019). The 2D nanomaterials mainly include lamellar graphene flakes (GRs) (Chun et al., 2017) and transition metal carbides/carbonitrides (MXenes) (Yang et al., 2020).

According to the integration manner of conductive materials on flexible substrates, multi-element conductive networks can be divided into ''multiple networks'' (Han et al., 2020; Huang et al., 2019; Zhao et al., 2019a) and ''hybrid networks'' (Liu et al., 2019b, 2019c; Shengbo et al., 2018). In multiple networks, each conductive material forms an independent, complete conductive network. The multiple networks are usually assembled by layer using coating methods (Ma et al., 2019) or prepared by mixing inside and coating outside the substrate simultaneously (Chen et al., 2016). For example, Cai et al. (Cai et al. (2018b) alternately deposited MXene and CNTs on a latex substrate using layer-by-layer spraying technology. Curled linear CNTs were likely used to knit loose MXene into a fabric, which significantly improved the order of the coating structure and conductive pathways, and it provided the sensor with a wider sensing range than using a single conductive material. Wang et al. (Wang et al. (2021a) found that the CNT conductive network mixed inside thermoplastic polyurethane (TPU) foam retained attractive continuity under high strain but exhibited extremely low sensitivity. After adsorbing a layer of MXene on the foam surface, the cracks that formed on the conductive coating caused the CNT/MXene multiple networks to have a GF value as high as 363.

In a hybrid network, different conductive materials jointly construct a single conductive network, which involves two compound modes. Most studies uniformly dispersed multiple conductive nanomaterials to form a hybrid network (Lu et al., 2019). For instance, Li et al. (Li et al. (2019) dip-coated printing paper in a CB/CNT suspension to prepare a strain sensor based on conductive paper. The CNT improved the dispersion of CBs and bridged the gaps between individual CB clusters to form a more stable hybrid network. A few studies assembled two conductive nanoparticles to create a new composite nanomaterial and then connected them to form a hybrid network (Pei et al., 2019). Zhang et al. (Zhang et al. (2017) used CNTs as templates to generate Ag nanoparticles, creating a new type of conductive nanomaterial with Ag nanoparticles coated around CNTs. Ag nanoparticles could be used as electronic bridges to connect CNTs, thereby reducing the contact resistance between the CNTs. This hybrid network effectively solved the problem of the poor linearity of CNT-based strain sensors.

Strain sensors containing multi-element conductive networks reported in the existing literature were mainly based on two conductive nanomaterials. There have been few studies on the performance and mechanism of ternary conductive networks. In addition, the previous research on the strain sensing mechanisms of multi-element conductive networks mainly focused on the synergistic effects of multiple conductive nanomaterials, but the effect of conductive nanomaterials with different dimensions on the properties of the conductive polymer nanocomposites and the strain sensing behaviors of multi-element networks have not been clarified.

In this article, a multidimensional carbon-based nanomaterial (MCN)/TPU nanofiber yarn (denoted as MCN/TPU-NY), which could be used as a strain sensor without post-processing, was prepared by multi-needle liquid-bath electrospinning and twisting after uniformly dispersing the MCN (including different combinations of 0D CBs, 1D CNTs, and 2D GRs) in the TPU spinning solution. Subsequently, the dispersion of MCNs, the morphologies and structures of the multi-element conductive networks, and the conductivity, mechanical properties, and strain sensing behaviors of MCN/TPU-NYs were compared and analyzed using different MCNs. Furthermore, the dimensional and synergistic effects of the nanomaterials and the optimal MCN were explored. Accordingly, the structural evolution of the ternary conductive network in the stretching process was revealed through electron microscopy technology and model simulations to further
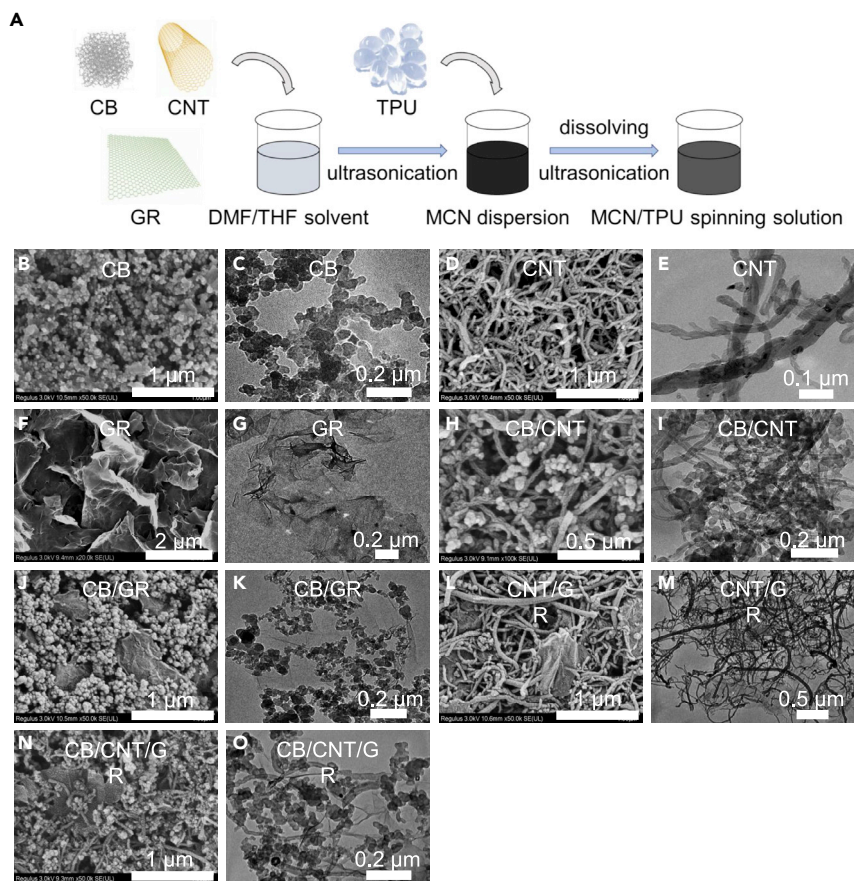
Figure 1. Production process and morphologies of MCN/TPU spinning solution
(A) Production process of MCN/TPU spinning solution. SEM and TEM images of MCNs: (B and C) CB, (D and E) CNT, (F and G) GR, (H and I) CB/CNT, (J and K) CB/GR, (L and M) CNT/GR, (N and O) CB/CNT/GR.

analyze the strain sensing mechanism. Finally, the function of a medicated plaster to detect motions during recovery from joint pain was realized by simply sewing the MCN/TPU-NY.

RESULTS

Structures and morphologies of MCN/TPU-NY

Good dispersibility of the MCN is a prerequisite for constructing a continuous conductive network inside the polymer matrix. Figure 1A schematically shows the production process of the MCN/TPU spinning solution. The dispersion states of various combinations of MCNs in the dimethylformamide (DMF)/tetrahydrofuran (THF) solvent was observed from the SEM and TEM images (Figures 1B–1O). Because of the strong van der Waals forces, the spherical CBs were not dispersed as individual particles but as aggregates containing several particles (Figures 1B and 1C). The linear CNTs curved and interwove into a structure similar to a web, but without significant entanglement (Figures 1D and 1E). The lamellar GRs overlapped one another like rice paper with distinct wrinkles (Figures 1F and 1G).

The dispersion characteristics of the MCNs did not change when they were compounded with each other. To highlight the sizes of the 0D CBs and the 1D CNTs, we specifically controlled the particle size of the CBs (30–45 nm) to be similar to the tube diameter of the CNTs (30–80 nm). For the CB/CNT nanocomposite, the CBs filled the pores in the CNT web, and interspersed CNTs acted as "bridges" connecting individual CB aggregates, forming typical "point–line" contact (Figures 1H and 1I). For the CB/GR, CNT/GR, and CB/CNT/GR nanocomposites, the CBs and CNTs were evenly spread on the lamellar GRs with large sizes, which acted as base maps, forming "point–face" and "line–face" contacts and filling the gaps between partially overlapped GRs. (Figures 1J–1O).
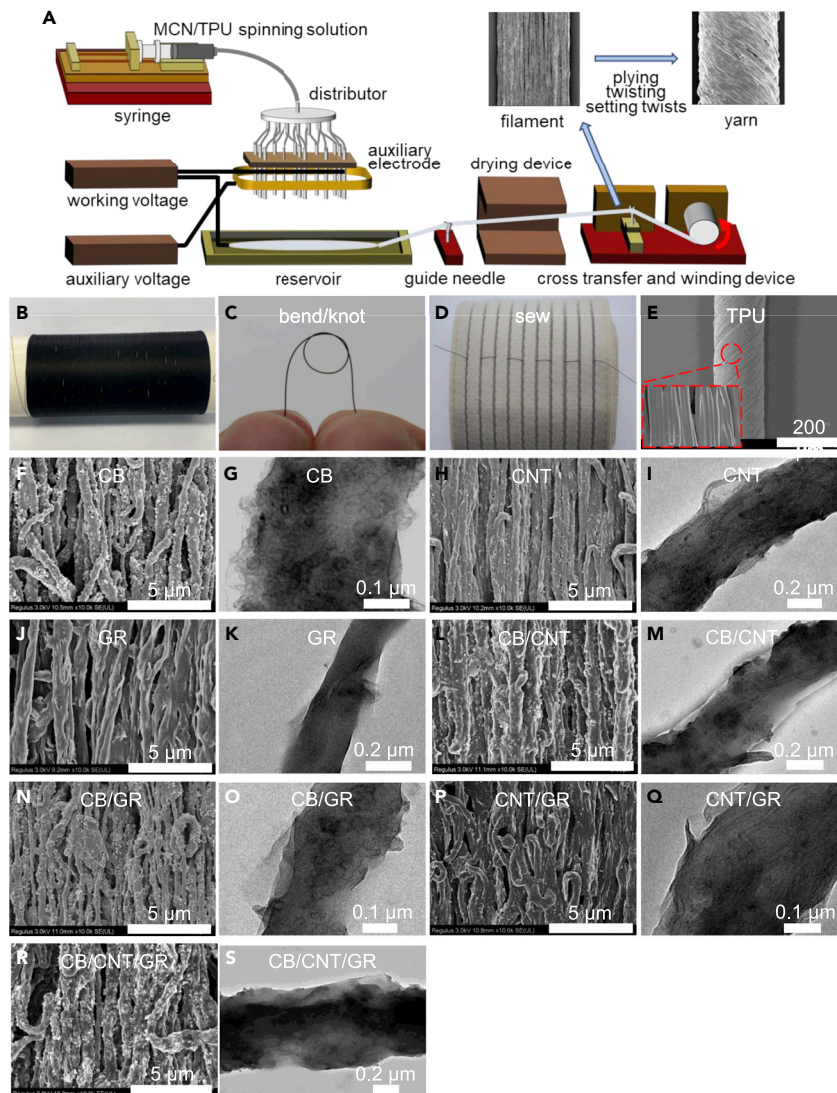
Figure 2. Production process and morphologies of MCN/TPU-NY

(A) Production process of MCN/TPU-NY.

(B) Optical images of MCN/TPU nanofiber filament.

(C and D) Optical images of MCN/TPU-NY.

(E) SEM image of the pure TPU nanofiber yarn. SEM and TEM images of composite nanofibers in MCN/TPU-NYs: (F and G) CB, (H and I) CNT, (J and K) GR, (L and M) CB/CNT, (N and O) CB/GR, (P and Q) CNT/GR, and (R and S) CB/CNT/GR.

Figure 2A schematically shows the production process of the MCN/TPU-NY. The MCN/TPU spinning solution was injected from the needles to form jets and then stretched to form nanofibers during the electrospinning. The MCNs formed conductive networks with special structures in the TPU-based nanofibers under the action of an electrostatic field. Figures 2B–2D reveal the optical graphs of the composite nanofiber filament and the MCN/TPU-NY, demonstrating that the filament could be manufactured continuously, and the highly flexible MCN/TPU-NY had a textile processing capacity. Because the MCNs were primarily distributed inside the TPU matrix, there were no concerns about the potential toxicity of the nanoparticles to the human body when the MCN/TPU-NY was in direct contact with skin (Li et al., 2012). The diameters of the pure TPU nanofibers with a smooth surface were about 500 nm, and parts of the nanofibers were glued together (Figure 2E).

No previous publication has systematically reported the dispersion characteristics of nanomaterials with different dimensions in nanofibers. Figures 2F–2S demonstrate the SEM and TEM images of MCN/TPU

composite nanofibers. The CBs were not completely uniformly dispersed inside the nanofibers but connected to form a chain-like network, and some CBs were embedded on the surfaces of the nanofibers like nut particles on Pocky biscuits (Figures 2F and 2G). Rather than being dispersed in a disordered manner in the solvent, the CNTs were aligned slightly along the axial direction inside the nanofibers because of the electrostatic field and the jet stretching in the process of electrospinning (Li et al., 2014). Because of the high aspect ratio, the CNTs were curved and interlocked inside the nanofibers, and parts of them were exposed outside the nanofibers, resembling tentacles (Figures 2H and 2I). Because the diameters of the nanofibers were smaller than those of the GRs (0.5–3 μm), flexible GRs were partially inserted diagonally into the nanofibers and partially attached to the surfaces of the nanofibers (Figures 2J and 2K). The contact characteristics of different nanomaterials inside the nanofibers were similar to those in the solvent (Figures 2L–2S).

Conductivity and mechanical properties of MCN/TPU-NY

From the microscopic scale, the total resistance of MCN/TPU-NY was a function of the intrinsic resistance of MCN and the layer resistance of TPU, which could be expressed as follows (Wang et al., 2021b):

$$R_t = \frac{M(R_a + R_s)}{N}, \qquad \text{(Equation 1)}$$

where R_t, R_a, and R_s were the total resistance, the resistance between two adjacent nanofillers, and the resistance across a single nanofiller, respectively. For MCN/TPU-NY, as R_a was much larger than R_s, the intrinsic resistance of MCN could be neglected ($R_a + R_s \approx R_a$). M was the number of nanofillers forming one conductive pathway and N was the number of conductive pathways, respectively. Thus, based on Simmons' tunneling theory, the total resistance was described as follows:

$$R_a = \frac{8\pi hd}{3sre^2} exp(rd), \quad r = \frac{4\pi}{h}\sqrt{2m_e\varphi}, \qquad \text{(Equation 2)}$$

then substituting Equation (2) into Equation (1) gave

$$R_t = \frac{M}{N}\left[\frac{8\pi hd}{3sre^2}exp(rd)\right], \qquad \text{(Equation 3)}$$

where h was the Plank's constant, s was the effective cross section, e was the electron charge, d was the average distance between adjacent conductive nanofillers, m_e was the electron mass and φ was and the height of tunneling potential barrier, respectively. Theoretically, compared with the unary conductive network, the resistance of the multi-element conductive composed of MCN should be smaller due to the higher values of N and s and the less value of d.

To explore the effect of MCNs on the properties of multi-element conductive networks, the conductivity, breaking stress, breaking elongation, elastic rebound, and mechanical hysteresis characteristics of the MCN/TPU-NYs containing CBs, CNTs, and GRs with different mass fractions were tested and analyzed. For brevity, the samples are referred to using an abbreviated notation. For example, "24CB/3CNT/3GR-Y" means an MCN/TPU-NY containing 24 wt.% CBs, 3 wt.% CNTs, and 3 wt.% GRs.

Figure S1A shows the conductivity of the unary networks of CB-Y, CNT-Y, and GR-Y. The conductivities of the MCN/TPU-NYs were improved by increasing the concentration of MCNs to form more conductive paths in the network. However, when the content of MCNs in the spinning solution reached 35 wt.% in the process of electrospinning, a large amount of charge was gathered at the highly conductive jet, which induced the opposite charge of the collector, leading to the separation of nanofibers from the collector. The spinning continuity was destroyed. In addition, for the conductivity of the solution is too high, the discharge phenomenon will occur, resulting in the failure of the flow pump. This phenomenon also occurred in the electrospinning of MXene/polyacrylonitrile nanofibers (Levitt et al., 2019). According to the conductivity–mass fraction curves, the CB network in the 30CB-Y was nearly saturated whereas the CNT network in the 30CNT-Y was far from saturated. Because of the limitation of the concentration of the GR dispersion, the maximum content of GRs in the GR-Y was 15 wt.%. When the content was 15 wt.%, the effects of the conductivity enhancement of three MCNs on the MCN/TPU-NYs were in the following order: GRs (2.37×10^{-3} S/cm) > CBs (2.14×10^{-5} S/cm) > CNTs (3.59×10^{-6} S/cm) because the face–face connection formed by overlapping 2D GRs had the largest contact area for electronic transmission. Although the connection types between the conductive nanomaterials in the CB network and the

CNT network were essentially both point contacts, there were more contact points between the 0D CBs than between the 1D CNTs under the same concentration.

The stress and elongation of the pure TPU nanofiber yarn were 75.4 MPa and 448%, respectively. Figures S1B and S1C show the breaking stress and breaking elongation curves, respectively, for the CB-Y, CNT-Y, and GR-Y. MCNs with high concentrations deteriorated the mechanical properties of the MCN/TPU-NYs by destroying the structure of the TPU matrix. As the concentration and size increased, the damage to the matrix caused by the MCNs was more significant. Surprisingly, 15 wt.% CBs did not significantly weaken the mechanical properties of the CB-Y, indicating that the 0D nanomaterial led to the least amount of damage to the structures of the nanofibers. In addition, the scaffold-shaped CNT network could enhance the stress of the CNT-Y at high concentrations. Although the GR had an efficient conductive reinforcement effect, it was inserted into the GR-Y like a razor blade because of the large-size sheet-like geometric structure. The stress and elongation of the 15GR-Y were only one-third and less than one-fourth of those of the 15CB-Y, respectively. Based on the conductivity and mechanical properties, the 0D CBs were the most ideal for constructing a unary network inside the MCN/TPU-NY. The CBs could increase the conductivity of the MCN/TPU-NY (0.212 S/cm) through a high loading, which was nearly 12 times higher than that of the pure TPU nanofiber yarn, and it had a negligible weakening effect on the mechanical properties.

The total content of the MCN was controlled at 30 wt.%, and the influence of the MCN on the properties of the MCN/TPU-NY containing the binary network was explored by adding an auxiliary filler to the main network. Limited by the spinning stability, the maximum content of GRs in the MCN/TPU-NY containing the binary network was 6 wt.%. Figure S2A shows the conductivity of the binary networks of CB/CNT-Y, CB/GR-Y, and GR/CNT-Y. When GR was the auxiliary filler, the conductivity of the CB/GR-Y decreased first and then increased with the increase in the GR content. Because of the constant total concentration of the binary network, there was a conductivity tradeoff for the CB/GR-Y, where a decrease in the main filler content weakened the conductivity and an increase in the auxiliary filler content strengthened the conductivity. Based on the conductivity result, the structural changes in the CB/GR binary networks mainly had three stages. When the concentration of the auxiliary filler was low (refer to 28.5CB/1.5GR-Y), the hybrid structure with more conductive paths formed by the auxiliary filler, the main filler was discontinuous in the binary network, and the decrease in the main filler content caused the conductivity of the CB/GR-Y to decline. When the concentration of the auxiliary filler reached the networked threshold (refer to 27CB/3GR-Y), the binary network was composed entirely of the hybrid structure, and a continuous auxiliary network was initially formed, which had a significant conductivity strengthening effect on the CB/GR-Y. Because the auxiliary network was dense enough to provide good electronic transmission capacity (refer to 24CB/6GR-Y), the binary network had the characteristics of a hybrid network and multiple networks simultaneously. Thus, the conductivity of the CB/GR-Y was significantly enhanced. The conductivity of the CNT/GR-Y showed the same characteristics as that of the CB/GR-Y.

When CNTs were the auxiliary filler, the conductivity of the CB/CNT-Y decreased first, then increased, and then decreased with the increase in the CNT content. The lengths of the CNTs were similar to the diameters of the GRs so the networked threshold of the CNTs was also 3 wt.%. When 1D CNTs and 2D GRs were used as auxiliary fillers, they were essentially in point contact with the 0D CBs in the main network. Thus, the conductivity of the 28.5CB/1.5CNT-Y was close to that of the 28.5CB/1.5GR-Y. After forming the CNT auxiliary network, the conductivity of the 27CB/3CNT-Y was higher than that of the 28.5CB/1.5CNT-Y but still lower than that of the 30CB-Y, and the conductivity of the CB/CNT-Y continued to decrease with the increase in the CNT content. When the CNT content was further increased to become the main network, the conductivity of the 18CNT/12CB-Y was more than three times that of the 24CNT/6CB-Y, indicating that the small-sized CBs only formed an auxiliary network when the content reached 12 wt.%. Even when the CB auxiliary filler was not networked, the conductivity of CNT/CB-Y increased first and then decreased with the increase in the CB content, and it was always higher than that of the 30CNT-Y. The conductivity of the 28.5CNT/1.5CB-Y was nearly five times higher than that of the 30CNT-Y. Compared to the structure with lamellar GRs bridging the CNTs in an overlaid mode, the structure with point-like CBs bridging CNTs in a filling mode had a stronger ability to increase the line–line contact in the main network and improve the dispersion of the CNTs. Thus, the conductivity of the 28.5CNT/1.5CB-Y was nearly five times higher than that of the 28.5CNT/1.5GR-Y. However, the bridging effect on the CBs and the electron transmission ability after forming the auxiliary network of the linear CNTs were inferior to those of the laminar GRs.

Figures S2B and S2C show the breaking stress and breaking elongation curves, respectively, for the CB/CNT-Y, CB/GR-Y, and GR/CNT-Y. Although GRs were the best at enhancing the conductivity of the binary network, the stress and elongation of the CB/GR-Y decreased significantly with the increase in the GR content. The same phenomenon was observed for the CNT/GR-Y. Therefore, the large-sized GR had a significant duality in their effect on the performance of the binary network. For the CB/CNT-Y, the auxiliary filler CNTs had a mechanical enhancement effect before forming an auxiliary network, which peaked when the CNTs were initially networked (refer to 27CB/3CNT-Y). However, as the CNT content further increased, the elongation of the CB/CNT-Y continued to decrease. This was because the CNTs had the highest degree of alignment in the nanofibers in the initial networked state. As the concentration increased, the content of non-oriented and crimped CNTs in the network increased, causing more damage to the nanofibers. When CBs were the auxiliary filler, the stress of the CNT/CB-Y deteriorated rapidly and then increased again with the increase in the CNT content. This also indicated that a high concentration of CNTs still had an enhancement effect on the stress of the yarn, which was consistent with the analysis results of the unary network. When CNTs were the main filler, the elongation of the CNT/CB-Y continued to decrease as the CNT content further increased.

According to the above results, CBs as the main filler endowed the MCN/TPU-NYs with excellent conductivities and good mechanical properties simultaneously, and CNTs and GRs as the auxiliary fillers had the effects of mechanical and conductivity reinforcement on the binary network, respectively. On this basis, the MCN/TPU-NY containing the ternary network with the best performance was explored by adjusting the concentrations of CBs, CNTs, and GRs (Figure S3). The influence of the auxiliary fillers, i.e., CNTs and GRs, on the performance of the CB/CNT/GR-Y was similar to that of the MCN/TPU-NY containing the binary network. Networked GRs could significantly enhance the conductivity of the CB/CNT/GR-Y, but they significantly reduced the mechanical properties. Un-networked CNTs played a role in enhancing the mechanical properties of the CB/CNT/GR-Y. After forming the CNT auxiliary network, the conductivity and mechanical properties of the CB/CNT/GR-Y both decreased with the increase in the CNT content. The conductivity of the 27CB/1.5CNT/1.5GR-Y was lower than that of the 30CB-Y but higher than those of the 28.5CB/1.5CNT-Y and 28.5CB/1.5GR-Y. This indicated that although the CNTs and GRs were not individually connected to form an auxiliary network, the ternary hybrid structure had more conductive paths than the binary hybrid structure. By comparison, it was found that after adding GRs to the CB/CNT binary network to form a ternary network, the conductivity of the MCN/TPU-NY improved, and the mechanical properties diminished. In particular, GRs significantly deteriorated the elongation of the CB/CNT/GR-Y when the content reached 6 wt.%. The elongation of the 21CB/3CNT/6GR-Y dropped by more than 60% compared to that of the 27CB/3CNT-Y and by nearly 50% compared to that of the 24CB/3CNT/3GR-Y. Therefore, the optimal content of GRs as a conductive reinforcement material was 3 wt.%.

After adding CNTs to the CB/GR binary network to form a ternary network, not only were the mechanical properties of the MCN/TPU-NY improved but the conductivity was also enhanced. The conductivity of the 24CB/3CNT/3GR-Y was even higher than that of the 24CB/6GR-Y. However, after adding CNTs to the CB unary network to form a binary network, the CNTs did not enhance the conductivity. This indicated that the CBs, CNTs, and GRs could form denser conductive paths by bridging with each other in the ternary network, and the GR auxiliary network could reduce the damage to the ternary network caused by the sparser CB main network. Because both the conductivity and mechanical properties of the CB/CNT/GR-Y decreased as the CNT content further increased, the optimal content of CNTs in the ternary network was 3 wt.%, which could provide both a mechanical enhancement and an additional conductivity enhancement.

The good elastic rebound and negligible mechanical hysteresis were the bases for the reproducibility and repeatability of the flexible strain sensor based on the MCN/TPU-NYs. The pure TPU nanofiber yarn and eight MCN/TPU-NY samples with total MCN concentrations of 30 wt.% and auxiliary filler concentrations of 3 wt.% were subjected to five stretch/release cycles at 50%, 100%, and 200% strains (if the sample had not broken) to assess the mechanical reliability (Figures S4A–S4I).

The deformation of the MCN/TPU-NY that could not recover after unloading to the initial state is called the residual strain (Yu et al., 2019a). Under the same strain, each cycle's loading and unloading paths were different, indicating that the MCN/TPU-NY underwent mechanical hysteresis (Chen et al., 2020). With the increase in the number of cycles, the residual strain of the MCN/TPU-NY increased, and the mechanical hysteresis decreased, which was most evident in the first cycle. These phenomena were attributed to the viscoelasticity of the TPU, the irreversible slip of the MCN in the strain process, and the lag of the network

reconstruction during unloading, which were consistent with previous reports on the cyclic behaviors of composites based on elastic copolymers such as polyurethane (Seyedin et al., 2014), styrene-butadiene-styrene (Wang et al., 2018), and polydimethylsiloxane (You et al., 2019).

To explore the influence of different conductive networks on the mechanical reliability of the MCN/TPU-NY, the elastic rebound and mechanical hysteresis characteristics of different MCN/TPU-NYs were quantitatively compared. The elastic recovery (ER) values of the MCN/TPU-NY samples under different strains were calculated as follows (Wang et al., 2018):

$$ER = \frac{\varepsilon - \varepsilon_R}{\varepsilon} \times 100\%,$$ (Equation 4)

where ε is the applied strain, and ε_R is the residual strain after five strain cycles. The mechanical hysteresis characteristics of the MCN/TPU-NY samples were compared by calculating the degree of hysteresis (DH) values as follows:

$$DH = \frac{A_{loading} - A_{unloading}}{A_{loading}} \times 100\%,$$ (Equation 5)

where $A_{loading}$ and $A_{unloading}$ are the areas of the loading and unloading curves in the fifth strain cycle, respectively.

The calculated values of ER and DH are shown in Figures S4J and S4K respectively. Compared with the pure TPU nanofiber yarn, the ER values of the MCN/TPU-NYs decreased and DH values increased after doping with MCN, which indicated that the conductive network reduced the mechanical reliability. The greater the strain was, the smaller the ER and the greater the DH of the MCN/TPU-NYs became. For the MCN/TPU-NY containing unary networks, the resilience and hysteresis of the 30CNT-Y were significantly inferior and superior to those of the 30CB-Y, respectively. During the stretching process, the linear CNTs slipped simply and underwent complicated untangling and re-entanglement, which significantly hindered the spring back of the MCN/TPU-NY. The ER and DH values of the 30CB-Y were close to and lower than those of the 15GR-Y, respectively. The ER and DH values of the 27CNT/3GR-Y were higher and lower than those of the 30CNT-Y, respectively. This indicated that the degrees to which the MCNs reduced the mechanical reliability of the MCN/TPU-NYs were in the order of CB < GR < CNT. Therefore, after adding the auxiliary filler CNTs or GRs to the CB main network, the ER of the MCN/TPU-NYs decreased, and the DH increased. In contrast, after adding the auxiliary filler CB or GR to the CNT main network, the ER increased and the DH decreased. The ER of the 24CB/3GR/3CNT-Y was higher than those of the 27CB/3CNT-Y and the 27CB/3GR-Y, indicating that the ternary network had a more stable structure.

To sum up, according to the conductivity and mechanical properties of the MCN/TPU-NYs (Figures S1–S4), CBs as the main filler endowed the MCN/TPU-NYs with satisfactory conductivity and mechanical properties simultaneously when the total content of the MCNs was controlled at 30 wt.% (Figure S1). When the contents reached 3 wt.%, CNTs, and GRs as the auxiliary fillers had the effects of mechanical and conductive reinforcement on the MCN/TPU-NYs, respectively, by forming an auxiliary network (Figure S2). For the MCN/TPU-NY containing a ternary network (Figure S3), CBs, CNTs, and GRs formed a denser hybrid network by bridging with each other, and 24CB/3CNT/3GR-Y showed the best performance (Table 1). The MCNs deteriorated the elastic rebound and enhanced the mechanical hysteresis of the yarn substrate, but a more stable conductive network could ameliorate this phenomenon (Figure S4).

Sensing behaviors of MCN/TPU-NY

For brevity, "24CB/3CNT/3GR-S" referred to a flexible strain sensor based on 24CB/3CNT/3GR-Y. According to the conductivity and mechanical property results, 30CB-S, 30CNT-S, 15GR-S, 27CB/3CNT-S, 27CB/3GR-S, 27CNT/3CB-S, 27CNT/3GR-S, and 24CB/3CNT/3GR-S were chosen to explore the effect of the MCNs on the strain sensing performances of the MCN/TPU-NYs.

The strain sensing performances of the MCN/TPU-NYs were characterized by the relative resistance change (RRC, defined by $\Delta R/R_0$, where ΔR is the change of resistance, and R_0 is the initial resistance of the sensor). Figure 3 shows the RRC–strain curves of the strain sensors containing unary, binary, and ternary conductive networks under monotonic strain. The slope of the curve represents the sensor's sensitivity. Table 2 shows the breaking strain (referring to the strain when the sensor broke), working strain (referring to the strain

Table 1. Conductivity and mechanical properties of MCN/TPU-NY samples

Sample	Conductivity (S/cm)	Breaking stress (MPa)	Breaking elongation (%)	Elastic recovery (%)	Mechanical hysteresis (%)
30CB-Y	0.126	67.2	289	76.3	38.6
27CB/3CNT-Y	0.115	75.52	322	76.3	41.4
27CB/3GR-Y	0.131	44.65	144	75.7	46
24CB/3CNT/3GR-Y	0.154	60.86	233	77	43.3

when the sensor lost its electrical signal), and RRC values at 50% and 100% strain for the strain sensors in Figure 3.

Because the RRC values of all the sensors increased exponentially with the strain, the strain sensing behaviors of the MCN/TPU-NYs mainly originated from the change of the tunneling resistance caused by the various distances between the MCNs under stretching (Yu et al., 2019b). Based on the tunneling effect model, RRC, variation of the number of conductive pathways (VCP), and variation of distance (VD) between adjacent MCNs in the MCN/TPU-NYs were quantitatively described as follows (Wang et al., 2021b):

$$RRC = (1 + A\varepsilon)\exp(w\varepsilon^n) - 1, \tag{Equation 6}$$

$$VD = 1 + A\varepsilon, \tag{Equation 7}$$

$$VCP = \exp(-w\varepsilon^n), \tag{Equation 8}$$

where A, w, and n were constants. A, w, and n were calculated from the fitting results of the experimental curves in Figure 3 and the model given by Equation (6), and the R^2 values are listed in Table 2. The model given by Equation (6) was consistent with the RRC values of the MCN/TPU-NYs. The R^2 of 24CB/3CNT/3GR-Y was the highest, indicating that the dispersion of MCNs in it was the best, and the separation of MCNs was more uniform under stretching. According to Equations (7) and (8), parameter A represents the rate of increase in distance of adjacent MCNs, and parameters w and n were related to the rate of decrease in conductive pathways. These three parameters reflect the strain sensitivity of the conductive networks composed of MCNs and could predict the sensing performances of the MCN/TPU-NYs. For 24CB/3CNT/3GR-Y, A was the highest and w was the lowest, indicating that the separation speed between the MCNs was the fastest under stretching because of the good dispersion, and the disconnection speed of the conductive network was the slowest because of the bridging effect of the three kinds of MCNs.

The differences in the strain sensing performances of the sensors depended not only on the conductivity and elongation of the MCN/TPU-NYs but also on the sensing mechanism of the multi-element conductive network composed of MCNs. First, the MCN/TPU-NYs containing unary conductive networks were compared (Figure 3A). The 30CB-S exhibited the maximum working strain and good linearity but low sensitivity because the CB network in the highly conductive 30CB-Y was saturated before stretching, and the disconnection process between spherical nanoparticles was simple and direct. The 30CNT-S had the highest sensitivity, but its response was extremely unstable under large strains. This was because the reduction
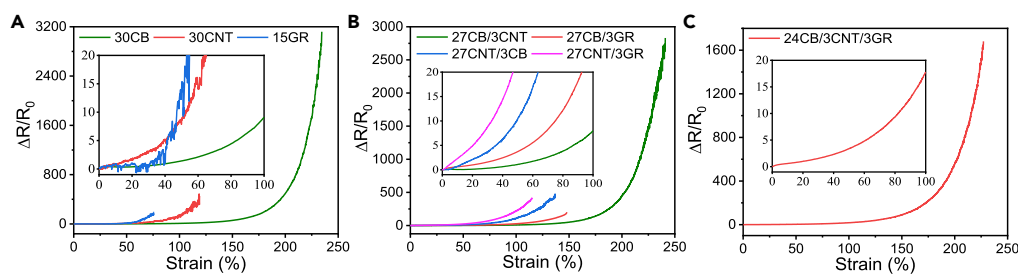

Figure 3. Monotonic strain sensing behaviors of MCN/TPU-NYs
RRC–strain curves of MCN/TPU-NYs: (A) 30CB-S, 30CNT-S, and 15GR-S.
(B) 27CB/3CNT-S, 27CB/3GR-S, 27CNT/3CB-S, and 27CNT/3GR-S.
(C) 24CB/3CNT/3GR-S.

Table 2. Breaking strain, working strain, and RRC values at 50% and 100% strain of the strain sensors and the calculated parameters of RRC model

Sample	30CB	30CNT	15GR	27CB/3CNT	27CB/3GR	27CNT/3CB	27CNT/3GR	24CB/3CNT/3GR
Breaking strain (%)	294	173	76	286	148	209	115	227
Working strain (%)	234	119	76	241	148	137	115	227
RRC of 50% strain	1.42	8.60	13.97	1.09	3.72	10.46	23.13	3.39
RRC of 100% strain	9.11	132.82	–	8.00	26.75	107.10	218.55	17.74
A	0.1757	4.5113	0.0198	0.0092	4.2789	1.0656	2.4549	5.8790
w	0.0138	0.0082	0.1580	0.1419	0.0015	0.2125	0.2437	0.0004
n	1.1828	1.3109	0.9337	0.7991	1.5411	0.6692	0.6335	1.7533
R^2	0.9962	0.9858	0.9984	0.9864	0.9966	0.9940	0.9961	0.9990

of the low-density point contact in the CNT network led to sudden variations in the resistance, and the unsaturated CNT network was more prone to failure. In the meantime, the linear CNTs were entangled and underwent a complex contact process under stretching. Although the conductivity of 15GR-S was close to that of 30CNT-S, its RRC was not measurable under small strains. Slip between the stacked GRs in the network slightly increased the contact resistance in this stage. Flexible GRs half-covered and were half inserted into the nanofibers, and their morphologies and locations changed irregularly under stretching. Thus, 15GR-S exhibited poor linearity. In addition, the breaking strain limited the working strain.

For the binary conductive networks (Figure 3B), the linearity of the strain sensor was improved by adding auxiliary fillers, i.e., CBs or GRs, to the CNT main network because of the transition from unstable "line–line" contact to the more-stable "line–point" and "line–surface" contact. Compared with the 30CNT-S, the working strain of the 27CNT/3CB-S became larger, indicating that the CBs filled between the CNTs play a bridging role when the CNT main network disconnected. Similarly, after adding the auxiliary filler CNTs to the CB main network, the working strain of the 27CB/3CNT-S also increased. After adding the auxiliary filler GRs to the CB or CNT main network, the RRC values of the strain sensors increased by about three times under 50 and 100% strains, but the working strain decreased. According to the results of the conductivity analysis, both the bridging effect and the auxiliary network of the GRs strongly enhanced the electronic transmission in the binary network. In the stretching process, the disconnection of the auxiliary network and the weakening of the bridging effect of the GRs drastically increased the sensor's resistance. According to the analysis of the mechanical properties, GRs significantly deteriorated the elongation of the MCN/TPU-NYs by destroying the polymer matrix. The working strain was the same as the breaking strain, indicating that the failure of the conductive networks in the 27CB/3GR-S and the 27CNT/3GR-S was because of the yarn fracture. By adding a second auxiliary filler, CNTs, to form a ternary network and improve the breaking strain of the MCN/TPU-NY, the 24CB/3CNT/3GR-S achieved the ideal working strain while maintaining the high sensitivity introduced by the GR (Figure 3C).

Before evaluating the dynamic responses and reliability of the strain sensors based on the CB main networks (30CB-S, 27CB/3CNT-S, 27CB/3GR-S, and 24CB/3CNT/3GR-S), the sensors were pre-stretched to a strain of 100% to improve the elastic rebound and mechanical hysteresis of the MCN/TPU-NYs and obtain more stable conductive networks. Figure 4A shows the RRC–strain curves of the four sensors in the first ten cycles of a periodic tension–release test with a strain of 50%. In the first cycle, the resistances of the three sensors other than the 24CB/3CNT/3GR-S increased monotonically in the tensile stage, after which they decreased first and then increased in the release stage, which is referred to as the "shoulder peak" phenomenon. Starting from the second cycle, the four sensors showed significant "double peaks" during loading and unloading. The inconsistency between the first and subsequent cycles and the difference in the responses to monotonic and cyclic strains indicated that parts of the conductive network broke irreversibly during the first tensile process, and the recovery of the conductive network was hysteretic during the release process (Li et al., 2020). With the increase in the number of cycles, the resistance response of the sensor first attenuated and then tended to be stable. Interestingly, the first cycle of the resistance response of the 24CB/3CNT/3GR-S was consistent with the subsequent cycles, and the RRC underwent almost no degradation, which indicated that the ternary conductive network had higher stability and reliability. This conclusion was consistent with the test results of the morphology and properties mentioned above.

The double-peaks behavior was mainly caused by the competition between the destruction and reconstruction of the conductive network (Christ et al., 2017). For the sensors based on the MCN/TPU-NYs,
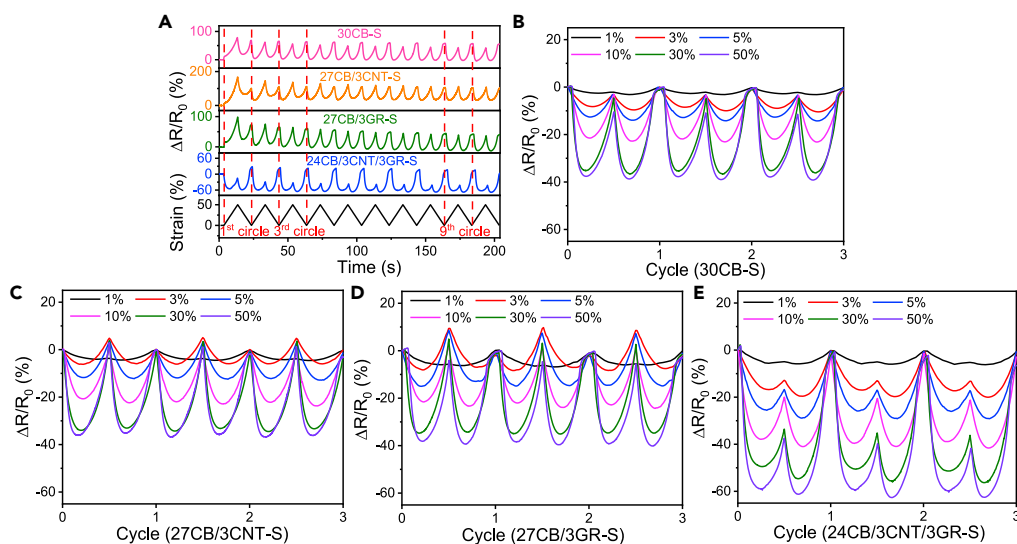
Figure 4. Cyclic strain sensing behaviors of MCN/TPU-NYs

(A) Dynamic responses of 30CB-S, 27CB/3CNT-S, 27CB/3GR-S, and 24CB/3CNT/3GR-S under the first ten cycles of periodic strain at a strain of 50%. RRCs under different cyclic strain amplitudes of (B) 30CB-S, (C) 27CB/3CNT-S, (D) 27CB/3GR-S, and (E) 24CB/3CNT/3GR-S.

the resistance response was characterized by double peaks with a larger absolute value of the RRC relative to the peak at the maximum strain. There were three reasons for the negative piezoresistive effect of the MCN/TPU-NYs. (1) Compared with a disordered state and a highly oriented state, the interconnection of the MCNs in the multi-element network was the most sufficient in the slightly oriented state, especially for linear CNTs. (2) In the tensile process, the Poisson effect of the MCN/TPU-NYs (squeezed or compressed in the direction perpendicular to the strain) reduced the distance between the MCNs inside the TPU matrix, thereby forming more conductive paths. (3) The nanofibers condensed more tightly when the MCN/TPU-NYs were stretched; so, the contact resistance between the MCNs exposed on the surfaces of the nanofibers was reduced.

Figures 4B–4E demonstrate the RRCs of the pre-stretched sensors over three cycles of a stable response in periodic strain tests with different maximum strains. Because it had good responses to small strains as low as 1% and large strains as high as 50%, the negative double peaks of the RRC became larger as the strain increased. The strain range and the strain dependence of the sensors meet the requirements of human physiology and motion signal detection (Kim et al., 2018). When the strain was only 1%, the resistances of the sensors only increased slightly at the maximum strain, indicating that the number of newly formed conductive paths in the conductive network under small strains was much higher than that of newly disconnected paths. When the strain increased from 30% to 50%, the absolute value of the RRC did not increase significantly, indicating that the destruction speed and the reconstruction speed of the conductive network were similar in this stage. In addition, for cyclic strains with different amplitudes, the location of the double peaks of the same sensor was not fixed but appeared at 20%–30% of the maximum strain. Therefore, in addition to the RRC of the double peaks in the sensing signal, the sensors could also detect strains based on the position of the double peaks, which greatly enhanced the accuracy. This unexpected phenomenon showed that the complex evolution of the destruction and reconstruction of the conductive networks was dynamic modulation.

Comparing the sensing behaviors of the strain sensors, the 30CB-S containing the CB conductive network with dense "point–point" connections showed a typical negative resistance response with double peaks to periodic strain (Figure 4B). After adding the auxiliary filler, i.e., CNTs or GRs, the basic models of the output signals of the 27CB/3CNT-S and the 27CB/3GR-S and the peak value of the double peaks did not change significantly, but there was a positive response spike at the maximum strain (Figures 4C and 4D). The disconnection of the auxiliary network greatly increased the resistance of the binary conductive network. The disconnection of the GR auxiliary network with a stronger conductivity enhancement effect damaged the binary conductive network more severely. After adding two auxiliary fillers, the peak value of the double peaks of the 24CB/3CNT/3GR-S increased by more than 1.5 times compared with those of the other three sensors, and the increase in the
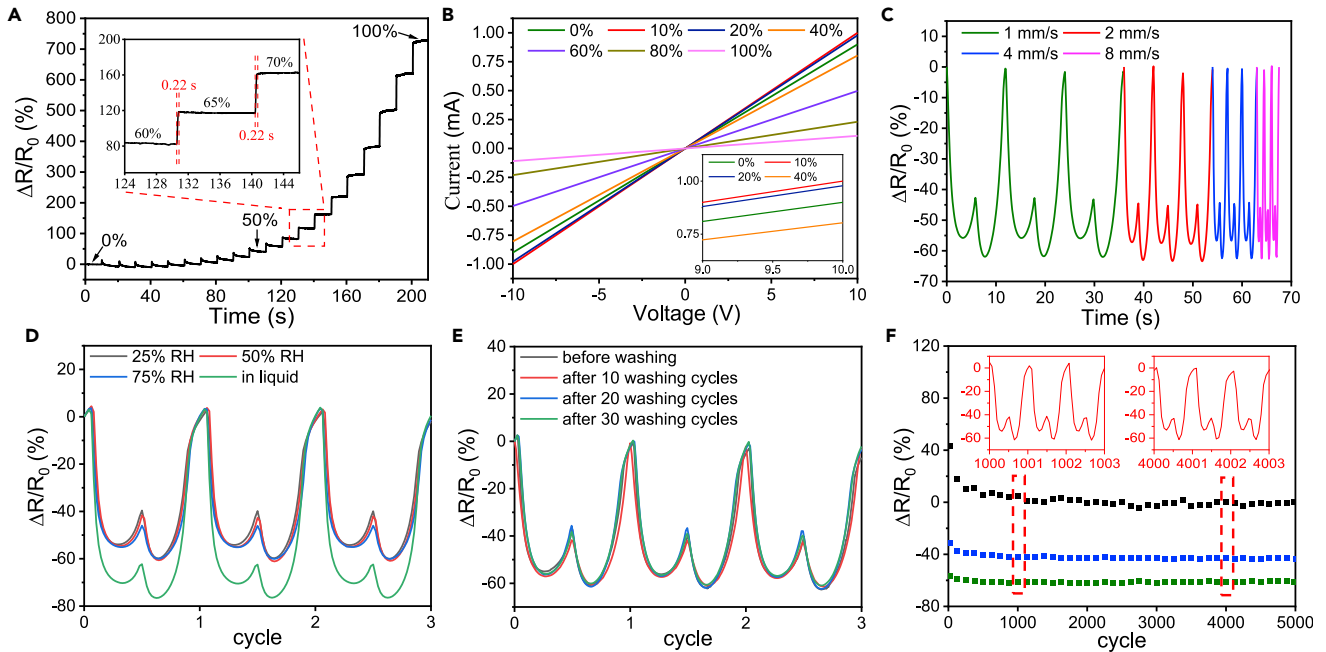
Figure 5. Strain sensing properties of 24CB/3CNT/3GR-S

(A) RRC under monotonic step strain from 0% to 100%; the inset shows the response time.

(B) I-V curves at different strains.

(C) RRCs under various cyclic strain rates at a strain of 50%.

(D) RRCs under different ambient humidity and in liquid at a strain of 50%.

(E) RRCs under the cyclic strain of 50% before and after washing.

(F) RRC under 5000 cycles of 50% strain.

resistance at the maximum strain decreased significantly, which weakened the double peak phenomenon (Figure 4E). Compared with the double peaks, the resistance response with a single peak is more convenient for the practical use of the sensor. When the sensor was stretched, the CBs, CNTs, and GRs formed more contacts and bridged with each other to avoid the disconnection of the conductive network. As a result, the 24CB/3CNT/3GR-S had a more significant negative piezoresistive effect.

To explore the structural evolution of the conductive network under static strain, the pre-stretched 24CB/3CNT/3GR-S was stretched step by step to 100% strain. In this quasi-transient step strain test, the loading speed was 100 mm/s, each level of strain was maintained for 10 s, and the strain interval was 5% (Figure 5A). When the strain was small, the reconstruction of the network prevailed. With the increase in strain, the destruction of the network gradually dominated. When the applied strain was above 60%, the RRC of the sensor was unchanged after a sudden increase, showing a stable positive piezoresistive effect. The static responses of the 24CB/3CNT/3GR-S to strains below 50% were inconsistent with the dynamic responses in Figure 4E, which was mainly attributed to the hysteresis of the conductive network reconstruction and the viscoelasticity of the TPU matrix. The 24CB/3CNT/3GR-S had a short response time of 220 ms (inset in Figure 5A). Current-voltage (I-V) characteristic curves for 24CB/3CNT/3GR-S at different strains are shown in Figure 5B. The resistance went down before it went up with the increased strain (from 0% to 100%) at a given voltage, which was consistent with the static responses in Figure 5A. Obviously, these linear I-V curves confirmed excellent ohmic behavior of 24CB/3CNT/3GR-S, demonstrating the stability of the ternary conductive network in a wide strain range.

The 24CB/3CNT/3GR-S output the same resistance responses to strains at different rates (Figure 5C). Humidity resistance and washable ability are essential for yarn sensors used in smart textiles. With the increase of humidity, the output signal of the 24CB/3CNT/3GR-S almost unchanged, although the main peak has an extremely slight decrease, proving the good sensing stability to humidity interference (Figure 5D). Interestingly, the negative RRC was significantly enhanced when the 24CB/3CNT/3GR-S worked in liquid. The main reason was that conductive water molecules penetrated into the yarn and filled the gaps between the nano-fillers in the ternary network to form a more stable quaternary network, thus forming more conductive paths
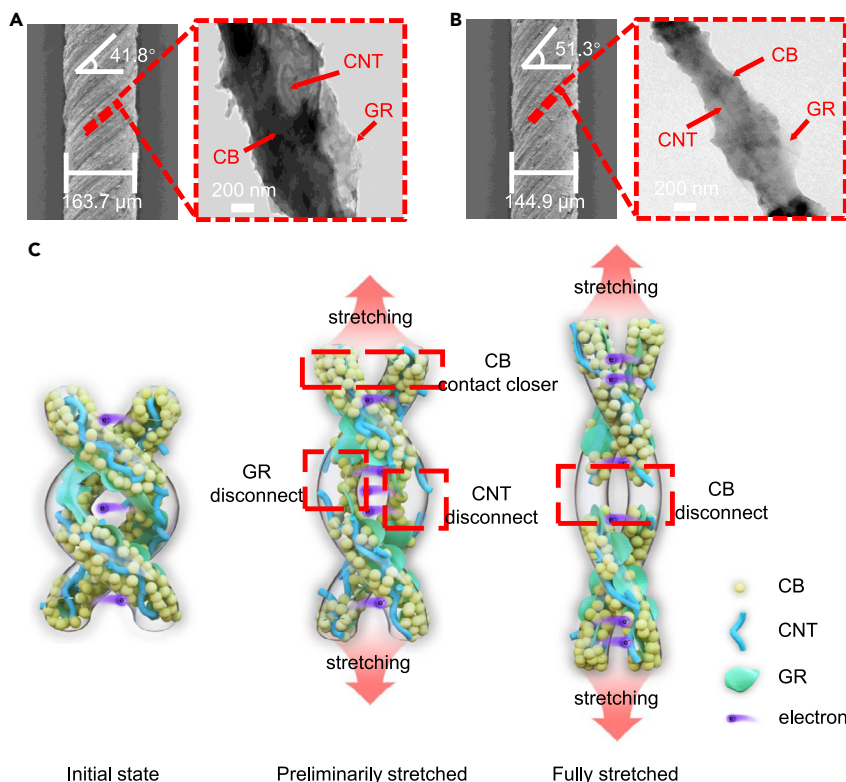
Figure 6. Structural evolution of the ternary conductive network
SEM images of 24CB/3CNT/3GR-Y and TEM images of inside nanofiber (A) before stretching and (B) after stretching. (C) Schematic illustration of structural evolution of ternary conductive network under stretching.

under stretching. The strain sensing behavior (Figure 5E) of the 24CB/3CNT/3GR-S did not change significantly after being washed 10, 20, and 30 times, indicating that it had ideal washability. It was perhaps that the large aspect ratio of the conductive networks was inside the nanofibers. The 24CB/3CNT/3GR-S was not sensitive to other forms of deformations, such as bending and torsion, which showed an unexpected anti-interference ability. Sensitivity to a single stimulation is conducive to signal decoupling and processing in the actual use of the sensor.

Furthermore, the 24CB/3CNT/3GR-S had good durability and repeatability over 5000 cycles for cyclic strains of 50% (Figure 5F) and 100% (Figure S5A). As can be seen from Figures S5B–S5D, the durability of 30CB-S, 27CB/3CNT-S, and 27CB/3GR-S under 50% strain were about 1700, 3100, and 370 cycles, respectively, which were much less than that of 24CB/3CNT/3GR-S. After a long-term loading cycle, the conductive network of 30CB-S deteriorated dramatically, the 27CB/3CNT-S directly lost efficacy and the 27CB/3GR-S with poor mechanical properties suddenly broke. It's worth noting that CNTs greatly enhanced the durability of the unary network of CBs, and the most stable ternary network had ideal fatigue resistance. These attractive properties make it an ideal candidate for strain sensors used in smart clothing.

Sensing mechanism of ternary conductive network

To further explore the strain sensing mechanism, the structural evolution of the ternary conductive network in the MCN/TPU-NY was revealed by SEM images of the 24CB/3CNT/3GR-Y and TEM images of the nanofibers inside the 24CB/3CNT/3GR-Y before stretching (Figure 6A) and after stretching (Figure 6B). Figure 6C shows a schematic illustration of the structural evolution of the ternary conductive network inside the MCN/TPU-NY under stretching.

In the initial stage, the dense 0D CBs with point–point contact inside the nanofibers formed the main network, and the 1D CNTs with high aspect ratios and 2D GRs with large diameters bridged the CB
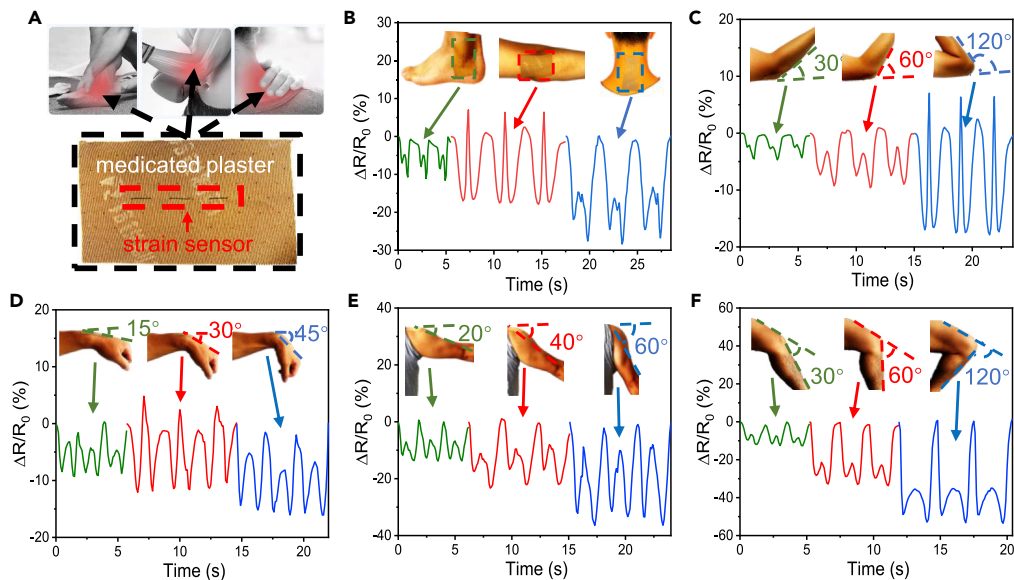
Figure 7. Application of 24CB/3CNT/3GR-S in smart medicated plasters
(A) Medicated plaster for the treatment of muscle and joint injuries and optical image of a smart medicated plaster sewn by 24CB/3CNT/3GR-S.
(B) Application of smart medicated plaster in detecting the bending of an ankle, elbow, and neck with maximum amplitude. Application of smart medicated plaster in detecting bending of various joints at different angles: (C) elbow, (D) wrist, (E) shoulder, and (F) knee.

particles in the form of "point–line–point" and "point–face–point," respectively, forming a hybrid network. Moreover, the CNTs and GRs were connected by line–line and "face–face" contact, respectively, forming two auxiliary networks, and they formed multiple networks together with the hybrid network. In addition, electrons could be transferred between the nanofibers via the MCN exposed at the nanofiber surface. After stretching, the nanofibers were elongated and thinner. The tunneling distance between high-concentration CBs decreased. The CNTs and GRs aligned and bridged more CBs. Therefore, the electron transport capacity of the hybrid network was enhanced. However, the low-concentration CNTs and GR auxiliary networks were disconnected, which caused the multiple networks to lose efficacy. Thus, the electrons in the nanofibers were transmitted only by the hybrid network.

The twist angle of the MCN/TPU-NY became smaller and the diameter decreased, indicating that the nanofibers condensed to become closer to each other after stretching, resulting in more conductive contact between the nanofibers. In summary, the ternary conductive network involved competition between the structural rearrangement of the hybrid network, which caused the network to become more stable, the auxiliary networks in the multiple networks to disconnect, and the contact resistance between the nanofibers to reduce. When the strain was sufficiently large, the damage to the hybrid network increased the resistance of the MCN/TPU-NY substantially.

Smart wearable application

Medicated plaster is a kind of traditional Chinese medicine that can be used to treat various conditions, such as ankle sprains, tennis elbow, and cervical spondylosis, by applying them to the affected area (Figure 7A). Excessive movement of the wounded area should be avoided during recovery from these muscle and joint injuries. 24CB/3CNT/3GR-S can be directly sewn into a medicated plaster to detect movement signals of the affected area and assist in rehabilitation. Figure 7B shows that the smart medicated plaster could sensitively detect the bending of an ankle, elbow, and neck by applying the medicated plaster to the skin. For the deformation of different joints, the output signals of the smart medicated plaster were significantly different. The bending angle of the ankle was the smallest; thus, the absolute value of the RRC of the double peaks was the smallest. The elbow could bend the most; thus, the RRC of the smart medicated plaster showed a positive spike at the maximum bending angle. Of interest, the RRC of the smart medicated plaster on the neck showed "triple peaks" when the head was bowed, which may have been because of the multi-segmented cervical

spine. In addition, the smart-medicated plaster could accurately detect deformations of different amplitudes of injured joints, such as the bending angle of the elbow, wrist, shoulder, and knee joints (Figures 7C–7F).

DISCUSSION

In this work, a highly stretchable and conductive MCN/TPU-NY was prepared with tensile strain sensing capabilities by multi-needle liquid-bath electrospinning and twisting. By comparing the properties and strain sensing behaviors of the MCN/TPU-NY fabricated using multi-element conductive networks composed of MCN, it was found that 0D CBs as the main filler could achieve a high conductivity at a high loading (30 wt.%) and maintain satisfactory mechanical properties, which endowed the sensor with a wide strain sensing range and good linearity. When the concentration reached the networked threshold (3 wt.%), 1D CNTs as the auxiliary filler could enhance the mechanical properties and strain sensing range but weakened the conductivity whereas 2D GRs as the auxiliary filler could enhance the conductivity and sensitivity but deteriorated the mechanical properties. The ternary conductive network had a more stable structure and exhibited better performances than the unary and binary conductive networks. Furthermore, the strain sensors with CBs as the main filler exhibited a negative piezoresistive effect and a double peak response to cyclic strain. The addition of two auxiliary fillers, i.e., CNTs and GRs, could enhance the negative piezoresistive effect, and weaken the double-peaks phenomenon, which is conducive to practical applications.

In accordance with the above, it was found that the ternary conductive network under stretching involved dynamic competition between the structural rearrangement of the hybrid network, the disconnection of the auxiliary network in multiple networks, and the reduction of the contact resistance between the nanofibers through electron microscopy technology and model simulations. For the MCN/TPU-NY containing 24 wt.% CBs, 3 wt.% CNTs, and 3 wt.% GRs, the conductivity was 0.154 S/cm, the breaking stress was 60.86 MPa, the maximum detectable strain was 227%, and the sensitivity at 100% strain was 17.74. In addition, the 24CB/3CNT/3GR-S exhibited a rapid response (220 ms), outstanding durability (5000 cycles of 50% and 100% strains), frequency independence, the anti-interference ability of humidity and other forms of strains, and washability. In general, compared with other strain sensors reported in the previous literature, 24CB/3CNT/3GR-S had advantages in all aspects of performance (Table S1). Finally, MCN/TPU-NY was directly integrated into a medicated plaster through simple sewing to detect the motion of injured areas, which could assist in rehabilitation.

Limitations of the study

The influences of the elastic polymer material characteristic, the conductive nanomaterial size, and the dispersant dosage on the performance of the flexible strain sensor remain to be explored. In addition, the sensitivity of the sensor needs to be further improved and the double-peaks phenomenon is not conducive to the practical use of the sensor. In future research, we aim to develop a high-performance strain-sensing ternary conductive network with a monotonic response and explore the sensing mechanism in more depth.

STAR★METHODS

Detailed methods are provided in the online version of this paper and include the following:

- KEY RESOURCES TABLE
- RESOURCE AVAILABILITY
  - ○ Lead contact
  - ○ Materials availability
  - ○ Data and code availability
- METHOD DETAILS
  - ○ Fabrication of MCN/TPU-NY
  - ○ Characterization of MCN/TPU-NY
- QUANTIFICATION AND STATISTICAL ANALYSIS

SUPPLEMENTAL INFORMATION

Supplemental information can be found online at https://doi.org/10.1016/j.isci.2022.105162.

REFERENCES

Cai, G., Yang, M., Pan, J., Cheng, D., Xia, Z., Wang, X., and Tang, B. (2018a). Large-scale production of highly stretchable CNT/Cotton/Spandex composite yarn for wearable applications. ACS Appl. Mater. Interfaces 10, 32726–32735. https://doi.org/10.1021/acsami.8b11885.

Cai, Y., Shen, J., Ge, G., Zhang, Y., Jin, W., Huang, W., Shao, J., Yang, J., and Dong, X. (2018b). Stretchable Ti3C2Tx MXene/carbon nanotube composite based strain sensor with ultrahigh sensitivity and tunable sensing range. ACS Nano 12, 56–62. https://doi.org/10.1021/acsnano.7b06251.

Chen, J., Zhang, J., Luo, Z., Zhang, J., Li, L., Su, Y., Gao, X., Li, Y., Tang, W., Cao, C., et al. (2020). Superelastic, sensitive, and low hysteresis flexible strain sensor based on wave-patterned liquid metal for human activity monitoring. ACS Appl. Mater. Interfaces 12, 22200–22211. https://doi.org/10.1021/acsami.0c04709.

Chen, S., Wei, Y., Yuan, X., Lin, Y., and Liu, L. (2016). A highly stretchable strain sensor based on a graphene/silver nanoparticle synergic conductive network and a sandwich structure. J. Mater. Chem. C Mater. 4, 4304–4311. https://doi.org/10.1039/c6tc00300a.

Christ, J.F., Aliheidari, N., Ameli, A., and Pötschke, P. (2017). 3D printed highly elastic strain sensors of multiwalled carbon nanotube/thermoplastic polyurethane nanocomposites. Mater. Des. 131, 394–401. https://doi.org/10.1016/j.matdes.2017.06.011.

Chun, S., Choi, Y., and Park, W. (2017). All-graphene strain sensor on soft substrate. Carbon 116, 753–759. https://doi.org/10.1016/j.carbon.2017.02.058.

Han, S., Liu, C., Lin, X., Zheng, J., Wu, J., and Liu, C. (2020). Dual conductive network hydrogel for a highly conductive, self-healing, anti-freezing, and non-drying strain sensor. ACS Appl. Polym. Mater. 2, 996–1005. https://doi.org/10.1021/acsapm.9b01198.

Huang, J., Li, D., Zhao, M., Mensah, A., Lv, P., Tian, X., Huang, F., Ke, H., and Wei, Q. (2019). Highly sensitive and stretchable CNT-bridged AgNP strain sensor based on TPU electrospun membrane for human motion detection. Adv. Electron. Mater. 5, 1900241. https://doi.org/10.1002/aelm.201900241.

Ichkitidze, L., Gerasimenko, A.Y., Podgaetsky, V., Selishchev, S., Dudin, A., and Pavlov, A.J.M.P. (2018). Electrical conductivity of the nanocomposite layers for use in biomedical systems. Mater. Phys. Mech. 37, 140–145.

Ichkitidze, L., Telishev, D., Demidenko, N., Kitsyuk, E., and Zar, V. (2019). The Study of the Electrical Conductivity of Layers of Biological Composite Nanomaterials1 (AIP Publishing LLC), p. 020029.

Kedambaimoole, V., Kumar, N., Shirhatti, V., Nuthalapati, S., Sen, P., Nayak, M.M., Rajanna, K., and Kumar, S. (2020). Laser-induced direct patterning of free-standing Ti3C2-MXene films for skin conformal tattoo sensors. ACS Sens. 5, 2086–2095. https://doi.org/10.1021/acssensors.0c00647.

Kim, I., Woo, K., Zhong, Z., Ko, P., Jang, Y., Jung, M., Jo, J., Kwon, S., Lee, S.H., Lee, S., et al. (2018). A photonic sintering derived Ag flake/nanoparticle-based highly sensitive stretchable strain sensor for human motion monitoring. Nanoscale 10, 7890–7897. https://doi.org/10.1039/C7NR09421C.

Lee, J., Kim, J., Liu, D., Guo, F., Shen, X., Zheng, Q., Jeon, S., and Kim, J. (2019). Highly aligned, anisotropic carbon nanofiber films for multidirectional strain sensors with exceptional selectivity. Adv. Funct. Mater. 29, 1901623. https://doi.org/10.1002/adfm.201901623.

Levitt, A.S., Alhabeb, M., Hatter, C.B., Sarycheva, A., Dion, G., and Gogotsi, Y. (2019). Electrospun MXene/carbon nanofibers as supercapacitor electrodes. J. Mater. Chem. A Mater. 7, 269–277. https://doi.org/10.1039/c8ta09810g.

Li, B., Luo, J., Huang, X., Lin, L., Wang, L., Hu, M., Tang, L., Xue, H., Gao, J., and Mai, Y.-W. (2020). A highly stretchable, super-hydrophobic strain sensor based on polydopamine and graphene reinforced nanofiber composite for human motion monitoring. Compos. B. Eng. 181, 107580.

Li, J., Tian, L., Pan, N., and Pan, Z.j. (2014). Mechanical and electrical properties of the PA6/SWNTs nanofiber yarn by electrospinning. Polym. Eng. Sci. 54, 1618–1624.

Li, Q., Liu, H., Zhang, S., Zhang, D., Liu, X., He, Y., Mi, L., Zhang, J., Liu, C., Shen, C., and Guo, Z. (2019). Superhydrophobic electrically conductive paper for ultrasensitive strain sensor with excellent anticorrosion and self-cleaning property. ACS Appl. Mater. Interfaces 11, 21904–21914. https://doi.org/10.1021/acsami.9b03421.

Li, X., Wang, L., Fan, Y., Feng, Q., and Cui, F.-z. (2012). Biocompatibility and toxicity of nanoparticles and nanotubes. J. Nanomater. 2012, 1–19. https://doi.org/10.1155/2012/548389.

Liu, F., Dong, Y., Shi, R., Wang, E., Ni, Q., and Fu, Y. (2020). Continuous graphene fibers prepared by liquid crystal spinning as strain sensors for Monitoring Vital Signs. Mater. Today Commun. 24, 100909. https://doi.org/10.1016/j.mtcomm.2020.100909.

Liu, H., Li, Q., Zhang, S., Yin, R., Liu, X., He, Y., Dai, K., Shan, C., Guo, J., Liu, C., et al. (2018a). Electrically conductive polymer composites for smart flexible strain sensors: a critical review. J. Mater. Chem. C Mater. 6, 12121–12141. https://doi.org/10.1039/c8tc04079f.

Liu, H., Xiang, H., Ma, Y., Li, Z., Meng, Q., Jiang, H., Wu, H., Li, P., Zhou, H., and Huang, W. (2018b). Flexible, degradable, and cost-effective strain sensor fabricated by a scalable papermaking procedure. ACS Sustain. Chem. Eng. 6, 15749–15755. https://doi.org/10.1021/acssuschemeng.8b04298.

Liu, H., Gao, H., and Hu, G. (2019a). Highly sensitive natural rubber/pristine graphene strain

sensor prepared by a simple method. Compos. B Eng. *171*, 138–145. https://doi.org/10.1016/j.compositesb.2019.04.032.

Liu, P., Liu, J., Zhu, X., Wu, C., Liu, Y., Pan, W., Zhao, J., Guo, X., Liu, C., Huang, Y., and Song, A. (2019b). A highly adhesive flexible strain sensor based on ultra-violet adhesive filled by graphene and carbon black for wearable monitoring. Compos. Sci. Technol. *182*, 107771. https://doi.org/10.1016/j.compscitech.2019.107771.

Liu, Y., Shi, X., Liu, S., Li, H., Zhang, H., Wang, C., Liang, J., and Chen, Y. (2019c). Biomimetic printable nanocomposite for healable, ultrasensitive, stretchable and ultradurable strain sensor. Nano Energy *63*, 103898. https://doi.org/10.1016/j.nanoen.2019.103898.

Lu, S., Ma, J., Ma, K., Wang, X., Wang, S., Yang, X., and Tang, H. (2019). Highly sensitive graphene platelets and multi-walled carbon nanotube-based flexible strain sensor for monitoring human joint bending. Appl. Phys. A *125*, 471. https://doi.org/10.1007/s00339-019-2765-8.

Ma, L., Yang, W., Wang, Y., Chen, H., Xing, Y., and Wang, J. (2018). Multi-dimensional strain sensor based on carbon nanotube film with aligned conductive networks. Compos. Sci. Technol. *165*, 190–197. https://doi.org/10.1016/j.compscitech.2018.06.030.

Ma, S., Tang, J., Yan, T., and Pan, Z. (2022). Performance of flexible strain sensors with different transition mechanisms: a review. IEEE Sens. J. *22*, 7475–7498. https://doi.org/10.1109/JSEN.2022.3156286.

Ma, Z., Xu, R., Wang, W., and Yu, D. (2019). A wearable, anti-bacterial strain sensor prepared by silver plated cotton/spandex blended fabric for human motion monitoring. Colloids Surf. A Physicochem. Eng. Asp. *582*, 123918. https://doi.org/10.1016/j.colsurfa.2019.123918.

Pei, Z., Liu, Y., Zhang, Q., Zhao, D., Wang, J., Yuan, Z., Zhang, W., and Sang, S. (2019). Highly sensitive, stretchable strain sensor based on Ag@COOH-functionalized CNTs for stroke and pronunciation recognition. Adv. Electron. Mater. *5*, 1900227. https://doi.org/10.1002/aelm.201900227.

Qureshi, Y., Tarfaoui, M., Lafdi, K.K., and Lafdi, K. (2019). Development of microscale flexible nylon/Ag strain sensor wire for real-time monitoring and damage detection in composite structures subjected to three-point bend test. Compos. Sci. Technol. *181*, 107693. https://doi.org/10.1016/j.compscitech.2019.107693.

Ryu, S., Lee, P., Chou, J.B., Xu, R., Zhao, R., Hart, A.J., and Kim, S.-G. (2015). Extremely elastic wearable carbon nanotube fiber strain sensor for monitoring of human motion. ACS Nano *9*, 5929–5936. https://doi.org/10.1021/acsnano.5b00599.

Seyedin, M.Z., Razal, J.M., Innis, P.C., and Wallace, G.G. (2014). Strain-responsive polyurethane/PEDOT:PSS elastomeric composite fibers with high electrical conductivity. Adv. Funct. Mater. *24*, 2957–2966. https://doi.org/10.1002/adfm.201303905.

Shengbo, S., Lihua, L., Aoqun, J., Qianqian, D., Jianlong, J., Qiang, Z., and Wendong, Z. (2018). Highly sensitive wearable strain sensor based on silver nanowires and nanoparticles. Nanotechnology *29*, 255202. https://doi.org/10.1088/1361-6528/aabbba.

Shi, W., Han, G., Chang, Y., Song, H., Hou, W., and Chen, Q. (2020). Using stretchable PPy@PVA composites as a high-sensitivity strain sensor to monitor minute motion. ACS Appl. Mater. Interfaces *12*, 45373–45382. https://doi.org/10.1021/acsami.0c14503.

Song, Y.X., Xu, W.M., Rong, M.Z., and Zhang, M.Q. (2019). A sunlight self-healable transparent strain sensor with high sensitivity and durability based on a silver nanowire/polyurethane composite film. J. Mater. Chem. A Mater. *7*, 2315–2325. https://doi.org/10.1039/c8ta11435h.

Sun, H., Dai, K., Zhai, W., Zhou, Y., Li, J., Zheng, G., Li, B., Liu, C., and Shen, C. (2019). A highly sensitive and stretchable yarn strain sensor for human motion tracking utilizing a wrinkle-assisted crack structure. ACS Appl. Mater. Interfaces *11*, 36052–36062. https://doi.org/10.1021/acsami.9b09229.

Tang, J., Wu, Y., Ma, S., Yan, T., and Pan, Z. (2022). Flexible strain sensor based on CNT/TPU composite nanofiber yarn for smart sports bandage. Compos. B Eng. *232*, 109605. https://doi.org/10.1016/j.compositesb.2021.109605.

Wang, H., Zhou, R., Li, D., Zhang, L., Ren, G., Wang, L., Liu, J., Wang, D., Tang, Z., Lu, G., et al. (2021a). High-performance foam-shaped strain sensor based on carbon nanotubes and Ti3C2Tx MXene for the monitoring of human activities. ACS Nano *15*, 9690–9700. https://doi.org/10.1021/acsnano.1c00259.

Wang, J., Lu, C., and Zhang, K. (2020). Textile-based strain sensor for human motion detection. Energy Environ. Mater. *3*, 80–100. https://doi.org/10.1002/eem2.12041.

Wang, X., Liu, X., and Schubert, D.W. (2021b). Highly sensitive ultrathin flexible thermoplastic polyurethane/carbon black fibrous film strain sensor with adjustable scaffold networks. Nano-Micro Lett. *13*, 64. https://doi.org/10.1007/s40820-021-00592-9.

Wang, X., Meng, S., Tebyetekerwa, M., Li, Y., Pionteck, J., Sun, B., Qin, Z., and Zhu, M. (2018). Highly sensitive and stretchable piezoresistive strain sensor based on conductive poly(styrene-butadiene-styrene)/few layer graphene composite fiber. Compos. Appl. Sci. Manuf. *105*, 291–299. https://doi.org/10.1016/j.compositesa.2017.11.027.

Wu, Y.-T., Yan, T., and Pan, Z.-J. (2021). Wearable carbon-based resistive sensors for strain detection: a review. IEEE Sens. J. *21*, 4030–4043. https://doi.org/10.1109/jsen.2020.3034453.

Yan, T., Wang, Z., Wang, Y.-Q., and Pan, Z.-J. (2018). Carbon/graphene composite nanofiber yarns for highly sensitive strain sensors. Mater. Des. *143*, 214–223. https://doi.org/10.1016/j.matdes.2018.02.006.

Yan, T., Zhou, H., Niu, H., Shao, H., Wang, H., Pan, Z., and Lin, T. (2019). Highly sensitive detection of subtle movement using a flexible strain sensor from helically wrapped carbon yarns. J. Mater. Chem. C Mater. *7*, 10049–10058. https://doi.org/10.1039/c9tc03065d.

Yang, H., Xiao, X., Li, Z., Li, K., Cheng, N., Li, S., Low, J.H., Jing, L., Fu, X., Achavananthadith, S., et al. (2020). Wireless Ti3C2Tx MXene strain sensor with ultrahigh sensitivity and designated working windows for soft exoskeletons. ACS Nano *14*, 11860–11875. https://doi.org/10.1021/acsnano.0c04730.

You, X., Yang, J., Wang, M., Hu, J., Ding, Y., Zhang, X., and Dong, S. (2019). Graphene-based fiber sensors with high stretchability and sensitivity by direct ink extrusion. 2D Mater. *7*, 015025. https://doi.org/10.1088/2053-1583/ab559f.

Yu, S., Wang, X., Xiang, H., Tebyetekerwa, M., and Zhu, M. (2019a). 1-D polymer ternary composites: understanding materials interaction, percolation behaviors and mechanism toward ultra-high stretchable and super-sensitive strain sensors. Sci. China Mater. *62*, 995–1004. https://doi.org/10.1007/s40843-018-9402-1.

Yu, Y., Zhai, Y., Yun, Z., Zhai, W., Wang, X., Zheng, G., Yan, C., Dai, K., Liu, C., and Shen, C. (2019b). Ultra-stretchable porous fiber-shaped strain sensor with exponential response in full sensing range and excellent anti-interference ability toward buckling, torsion, temperature, and humidity. Adv. Electron. Mater. *5*, 1900538. https://doi.org/10.1002/aelm.201900538.

Yue, X., Jia, Y., Wang, X., Zhou, K., Zhai, W., Zheng, G., Dai, K., Mi, L., Liu, C., and Shen, C. (2020). Highly stretchable and durable fiber-shaped strain sensor with porous core-sheath structure for human motion monitoring. Compos. Sci. Technol. *189*, 108038. https://doi.org/10.1016/j.compscitech.2020.108038.

Zhang, Q., Liu, L., Zhao, D., Duan, Q., Ji, J., Jian, A., Zhang, W., and Sang, S. (2017). Highly sensitive and stretchable strain sensor based on Ag@CNTs. Nanomaterials *7*, E424. https://doi.org/10.3390/nano7120424.

Zhao, D., Zhang, Q., Liu, Y., Zhang, Y., Guo, X., Yuan, Z., Zhang, W., Zhang, R., Lian, J.W., and Sang, S. (2019a). Highly sensitive and flexible strain sensor based on AuNPs/CNTs' synergic conductive network. Appl. Nanosci. *9*, 1469–1478. https://doi.org/10.1007/s13204-019-00959-w.

Zhao, M., Li, D., Huang, J., Wang, D., Mensah, A., and Wei, Q. (2019b). A multifunctional and highly stretchable electronic device based on silver nanowire/wrap yarn composite for a wearable strain sensor and heater. J. Mater. Chem. C Mater. *7*, 13468–13476. https://doi.org/10.1039/c9tc04252k.

Zheng, Q., Lee, J.-h., Shen, X., Chen, X., and Kim, J.-K. (2020). Graphene-based wearable piezoresistive physical sensors. Mater. Today *36*, 158–179. https://doi.org/10.1016/j.mattod.2019.12.004.

STAR★METHODS

KEY RESOURCES TABLE

REAGENT or RESOURCE	SOURCE	IDENTIFIER
Chemicals, peptides, and recombinant proteins		
Conductive carbon black	Nanjing XFNANO Materials Tech Co., Ltd., China	Model XFI15, grain size of 30–45 nm
Dispersant	Nanjing XFNANO Materials Tech Co., Ltd., China	Model XFZ22
N,N-dimethylformamide	Sinopharm Group Chemical Reagent Co. Ltd., China	CAS number: 68-12-2, purity ≥99.0%
Tetrahydrofuran	Jiangsu Enox Functional Chemical Co., Ltd, China	CAS number: 109-99-9, purity ≥99.5%
Carbon nanotube/N,N-dimethylformamide dispersion	Chengdu Organic Chemicals Co. Ltd., China	Model TNDDM-M8, the length, diameter, and content of CNTs were <10 μm, 30–80 nm, and 10 wt.%, respectively
Graphene/N,N-dimethylformamide dispersion	Chengdu Organic Chemicals Co. Ltd., China	Model TNDPRGO, the thickness, diameter, and content of GR were 0.55–3.74 nm, 0.5–3 μm, and 2 wt.%, respectively
Thermoplastic polyurethane	BASF Co., Ltd	Elastollan 1195A
Software and algorithms		
Image-ProPlus 6.0	Media Cybernetics	www.mediacy.com
Origin 2021	OriginLab	www.originlab.com
Other		
Magnetic stirrer	Shanghai EXCEED Instrument Equipment Co., Ltd, China	Model HJ-6
Ultrasonic cleaner	Ningbo Scientz Biotechnology Co., China	Model SB-5200D
Cold field-emission scanning electron microscopy	HITACHI Co.	Model Regulus-8100
Field-emission transmission electron microscopy	FEI Co.	Model Tecnai G20
Universal testing machine	INSTRON Co.	Model Instron 3365
Digital multi-meter	FLUKE Co.	Model F17B+
Electrochemical workstation	CH Instruments Inc.	Model CHI760E
Sample dyeing machine	Wuxi Yangbo Textile Equipment Co., Ltd	Model M-7-18P

RESOURCE AVAILABILITY

Lead contact

Further information and requests for resources and reagents should be directed to and will be fulfilled by the lead contact, Prof. Zhijuan Pan (zhjpan@suda.edu.cn).

Materials availability

This study did not generate new unique reagents.

Data and code availability

- All data reported in this article will be shared by the lead contact on request.

- This article does not report original code.

- Any additional information required to reanalyze the data reported in this article is available from the lead contact on request.

METHOD DETAILS

Fabrication of MCN/TPU-NY

CBs, CNTs, and GRs were first dispersed in a DMF/THF mixed solvent using a magnetic stirrer for 10 min and then subjected to ultrasonication for 2.5 h in an ultrasonic cleaner. The mass of the dispersant added simultaneously was 0.2 times that of the CBs, and the mass of THF was 0.25 times that of DMF in the mixed solvent. TPU was then dissolved in the dispersion with continuous stirring for 12 h to prepare an MCN/TPU composite solution containing 9 wt.% TPU. The spinning solution was further ultrasonicated for 2 h before electrospinning.

The process for producing an MCN/TPU-NY was the same as that in our group's previous work (Tang et al., 2022). The spinning parameters were as follows: ambient humidity of 30% ± 5% RH, a flow rate of 4 mL/h, receiving distance of 24 cm, working voltage of 33 kV, an auxiliary voltage of 24 kV, and winding speed of 120 m/h. The twisting parameters were selected as a ply number of six filaments, 2500 twists per meter, twist setting temperature of 150°C, and setting time of 60 min.

Various conductive networks (CB, CNT, GR, CB/CNT, CB/GR, CNT/GR, and CB/CNT/GR) were constructed inside the MCN/TPU-NY. The MCN/TPU-NY could be directly used as a strain sensor without post-processing, such as using silver glue to fabricate electrodes (Cai et al., 2018a; Sun et al., 2019) or encapsulation with an elastic polymer (Liu et al., 2020; Ryu et al., 2015).

Characterization of MCN/TPU-NY

The morphologies of the samples were observed using cold field-emission scanning electron microscopy (SEM) and field-emission transmission electron microscopy (TEM). The TEM samples were prepared by ultrasonically dispersing the powder cut from the de-twisted yarn in ethanol and then using a pipette to drop the dispersion onto a carbon support film. The diameters of the yarns were measured in the SEM images using an image analyzer.

The mechanical properties of the yarns were tested using a universal testing machine with a length of 50 mm and a drawing speed of 50 mm/min. A digital multi-meter was used to test the resistances of the yarns. In testing the performances of the strain sensors based on 3 cm of the MCN/TPU-NY, the strain loading was implemented with a universal testing machine.

To obtain the resistance variations, a constant voltage (0.1 V) was applied to the strain sensors to acquire a real-time current signal using an electrochemical workstation. In washing tests, the MCN/TPU-NY was washed 30 times at 40°C in a sample dyeing machine with a low liquor ratio using a conventional cleaning agent. After each 10 washing cycles, the conductivity and strain sensing behavior were measured. Informed written consent from all of the participants was obtained before the tests of the smart wearable device.

QUANTIFICATION AND STATISTICAL ANALYSIS

The average value and standard deviation of MCN/TPU-NY's diameter were calculated by 50 measurements. The average value and standard deviation of MCN/TPU-NY's conductivity and mechanical properties were calculated by 10 measurements. Strain sensing performances were tested using different batches of MCN/TPU-NY. All the statistical data were processed through the Origin software.